AGU PUBLICATIONS

JGR

Journal of Geophysical Research: Oceans

RESEARCH ARTICLE

10.1002/2015JC011207

Key Points:
- HF Doppler radar observed currents from the 2011 Tohoku tsunami south of Oahu
- Model hindcast agrees with observed resonance modes over Penguin Bank

Correspondence to:
L. R. Benjamin,
lrb@hawaii.edu

Citation:
Benjamin, L. R., P. Flament, K. F. Cheung, and D. S. Luther (2016), The 2011 Tohoku tsunami south of Oahu: High-frequency Doppler radio observations and model simulations of currents, *J. Geophys. Res. Oceans*, *121*, 1133–1144, doi:10.1002/2015JC011207.

Received 6 AUG 2015
Accepted 6 JAN 2016
Accepted article online 12 JAN 2016
Published online 5 FEB 2016

The 2011 Tohoku tsunami south of Oahu: High-frequency Doppler radio observations and model simulations of currents

L. R. Benjamin[1], P. Flament[1], K. F. Cheung[2], and D. S. Luther[1]

[1]Department of Oceanography, University of Hawaii at Manoa, Honolulu, Hawaii, USA, [2]Department of Ocean and Resources Engineering, University of Hawaii at Manoa, Honolulu, Hawaii, USA

Abstract A 16 MHz high-frequency Doppler radio (HFDR) deployed on the south shore of Oahu (Hawaii) detected oscillatory radial currents following the arrival of the 2011 Tohoku tsunami. The observations over a two-dimensional area provided an opportunity for intercomparison with the spatial patterns of currents and the resonant modes predicted by a nonhydrostatic model. Over the 50 m deep Penguin Bank, extending west from Molokai, the observed currents are intensified in two areas: 43 min period currents of 0.27 m s^{-1} lasting 6 h are observed on the south part of the bank, while 27 min period currents of 0.14 m s^{-1} lasting 2 h are observed on the north. The spatial EOFs suggest that standing full-waves and 3/2 waves formed over the bank. Modeled currents over Penguin Bank are similar to the observations but their north-south asymmetry is less pronounced than observed. Nearshore, observed alongshore currents showed long-period oscillations of 43 min that stretched along the entire coastline, while modeled currents show strong evidence for edge waves. EOF analysis of the nearshore signal suggests that the HFDR and model reveal different processes. The discrepancy might be attributed to the fact that both the Penguin Bank and nearshore observations are limited by HFDR sensitivity to azimuthal sidelobe contamination and decreased angular resolution at high steering angles.

1. Introduction

On 11 March 2011 at 05:46 UTC, a moment-magnitude 9.0 earthquake struck Japan, with an epicenter 140 km east of Sendai and 373 km northeast of Tokyo. The earthquake involved a 200 km long section of the Eurasian plate sliding up to 60 m along a 10° incline over the subducting Pacific Plate and generated a large tsunami [*Yamazaki et al*., 2011a]. The sea level measurement nearest to the epicenter, the Deep-ocean Assessment and Reporting of Tsunamis (DART) buoy 21418, recorded a 1.75 m high tsunami wave in 4000 m of water. The near-field tsunami devastated the northeast coast of the island of Honshu, with maximum runup of 39.7 m near Miyako and inundation greater than 5 km on the Sendai Plain [*Mori et al*., 2011]. Nearly 16,000 people were killed, and almost 3000 are still missing [*National Police Agency of Japan*, 2011]. The total damage in Japan is estimated at $156–$244 billion [*Mimura et al*., 2011].

Though not as devastating as the near-field tsunami, the far-field tsunami caused damage around the Pacific. In the Kuril Islands, a building was flooded and ice deposited on the beaches [*Kaistrenko et al*., 2013]. In New Zealand, several harbors and vessels suffered minor damage [*Borrero et al*., 2013]. In the Galapagos Islands, several buildings and coastal properties were flooded [*Lynett et al*., 2013]. There was some damage along the West Coast of the United States, particularly to harbors and vessels as even small wave amplitudes can cause swift currents [*Allan et al*., 2012]. In Hawaii, strong currents damaged over 200 small vessels in Keehi Lagoon and some dock facilities; total damage was estimated at $30 million [*Dunbar et al*., 2011; *Fiedler et al*., 2014].

Strong currents caused most of the damage in Hawaii. Despite the dangers posed by tsunami currents, they have not been monitored until recently because the unpredictable generation of tsunamis precludes the timely deployment of current meters. Fortuitous detection of tsunami currents with acoustic Doppler current profilers (ADCPs) allowed point comparison of modeled currents [*Yamazaki et al*., 2012; *Cheung et al*., 2013; *Zhou et al*., 2014], but were fairly sparse; 25 point-measurement instruments were used to validate one tsunami model for the whole ~70,000 km^2 area surrounding the main Hawaiian Islands [*Cheung et al*., 2013]. There have been no two-dimensional spatial comparisons of currents near the coast needed to validate model results, important for maritime hazard mapping.

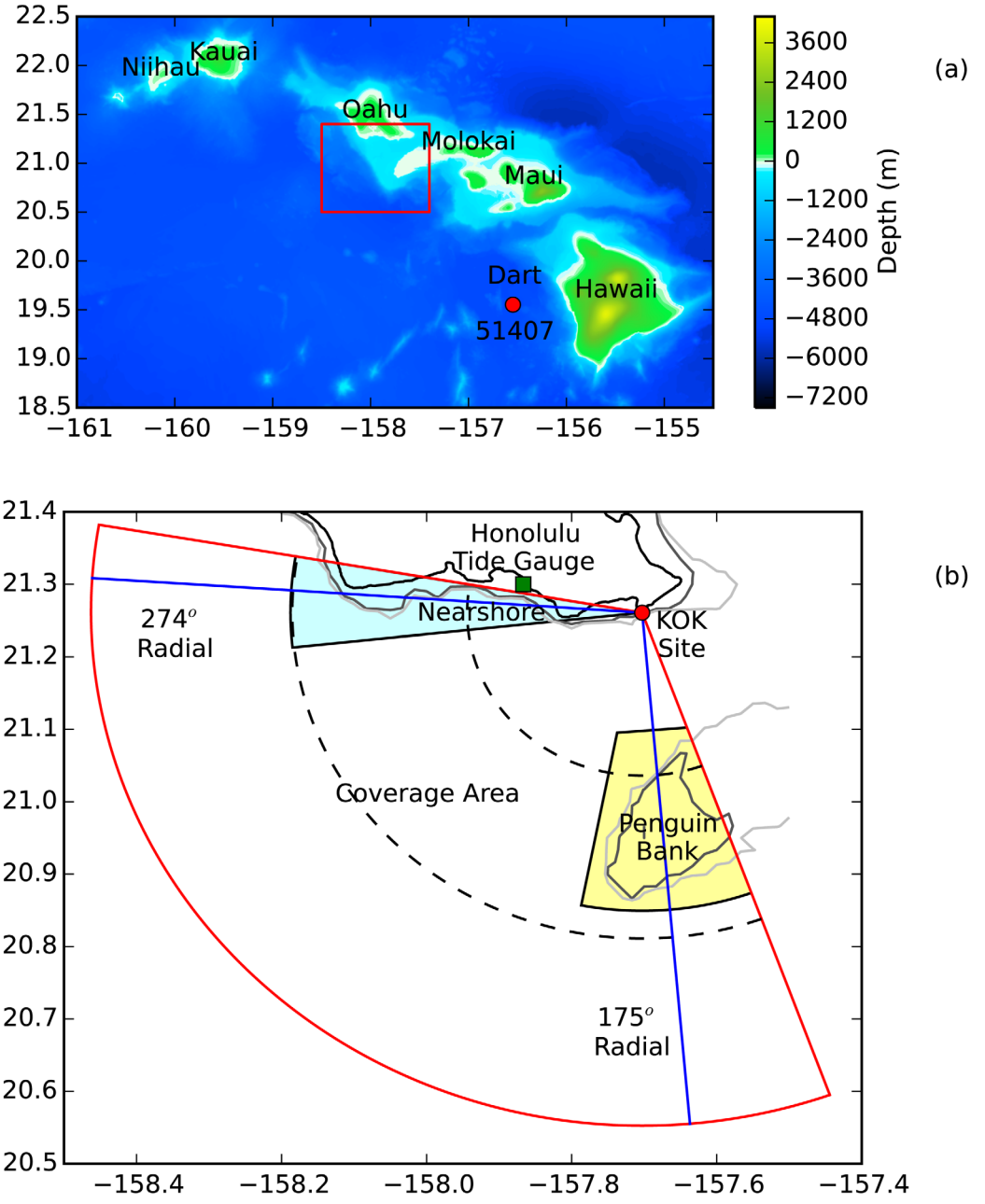

Figure 1. Map of the (a) Hawaiian Islands showing the location of DART 51407. The area within the red box, enlayed in Figure (1b), is the main study area. Also shown are the areas over which EOFs were computed. Range rings indicate 25, 50, and 75 km.

High-frequency Doppler radios (HFDRs) can map surface currents over an area, measuring the surface current radial to the instrument. Theoretical studies of the HFDR backscatter [*Gurgel et al.*, 2011; *Grilli et al.*, 2015] and particle velocities [*Lipa et al.*, 2006] have shown its potential for mapping tsunami currents, a concept first proposed by *Barrick* [1979]. The HFDR measurement volumes are small (∼1 km in range, ∼10° in azimuth, ∼1 m in depth) relative to the wavelength of tsunamis so the currents within the volumes are relatively homogeneous.

Wave shoaling increases particle velocity, enabling detection of tsunami currents by HFDRs in shallow areas, which may further exhibit signs of resonance if energy is trapped. The 2011 Tohoku tsunami was detected by HFDR in Chile [*Dzvonkovskaya et al.*, 2011], multiple locations along the U.S. West Coast and Japan [*Lipa et al.*, 2011, 2012], and in the Kii Channel in Japan [*Hinata et al.*, 2011]. These data sets were either insufficient to

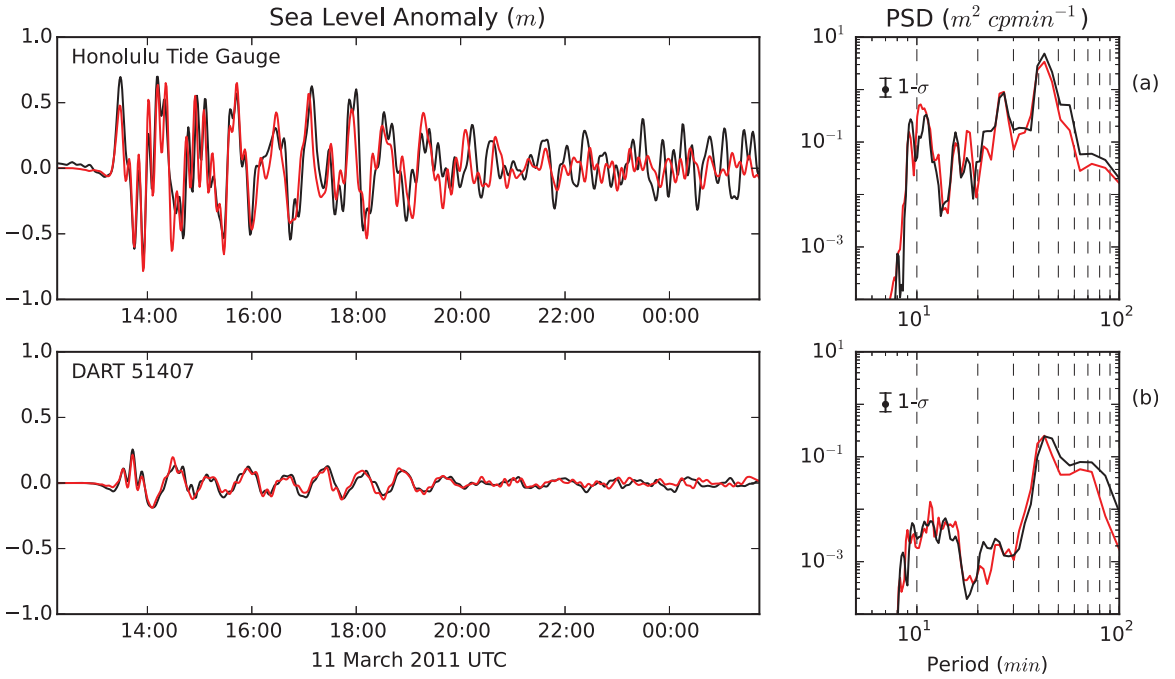

Figure 2. (left) Sea level anomalies and (right) PSDs from the (a) Honolulu tide gauge and (b) DART 51407. The red lines are from the model, and the black lines are from observations.

study resonance, or no such attempts were made despite model evidence for resonance [e.g., *Yamazaki and Cheung*, 2011; *Yamazaki et al.*, 2013].

During the Tohoku tsunami, an HFDR was operational on Oahu's southeastern shore. Its coverage extended beyond the shallow (50 m) Penguin Bank 20–40 km to the southeast. These observations provided an opportunity to detect currents excited by the tsunami, analyze the patterns of resonance, and inter compare with a model hindcast. Uniform incoming wavefronts are not expected because waves are scattered by the Northwest Hawaiian Islands [*Yamazaki et al.*, 2012]. Instead, the resonant response and subsequent trapping of tsunami energy are expected to dominate in the Hawaiian Islands. Previous models of tsunami responses have shown strong, prolonged, and complex resonant oscillations that depended less on the characteristics of individual tsunamis and more on the natural resonant modes of the region [e.g., *Munger and Cheung*, 2008; *Roeber et al.*, 2010; *Yamazaki and Cheung*, 2011]. Several of the modes described have strong antinodes over Penguin Bank or along Oahu's south shore [*Munger and Cheung*, 2008, Figures 2 and 4]. Because the maximum of spectral amplitude lies over Penguin Bank, it is a place to probe for resonant activity in the islands.

In this paper, we provide an intercomparison of the recorded HFDR currents of the Tohoku tsunami with the model results of *Cheung et al.* [2013]. The model results, which have been validated by point measurements of surface elevation and current around the Hawaiian Islands, exhibit strong resonance oscillations over Penguin Bank. Section 2 describes the data and methodology. Section 3 contains the results and the discussion. Section 4 concludes the study and makes recommendations for future work.

2. Data and Methods

The WERA HFDR [*Gurgel et al.*, 1999a, 1999b] at Koko Head (KOK) detected radial currents south of Oahu during the 2011 Tohoku tsunami (Figure 1) through the Bragg frequency. The Doppler shift of electromagnetic waves Bragg-scattered by surface waves has two parts: one from the phase speed of the scattering ocean waves, and a second from the surface currents. The 12 element receive array operated at 16.13 MHz with a range of about 100 km and boresight at 221°. Four times hourly, 11.2 min of data with 2048 chirps were gathered. The data were processed by breaking the 2048 chirps into half-overlapping 4.2 min periods of 768 chirps. Radial velocity is the difference between theoretical waves-only and observed waves-plus-currents Bragg frequencies, Δf,

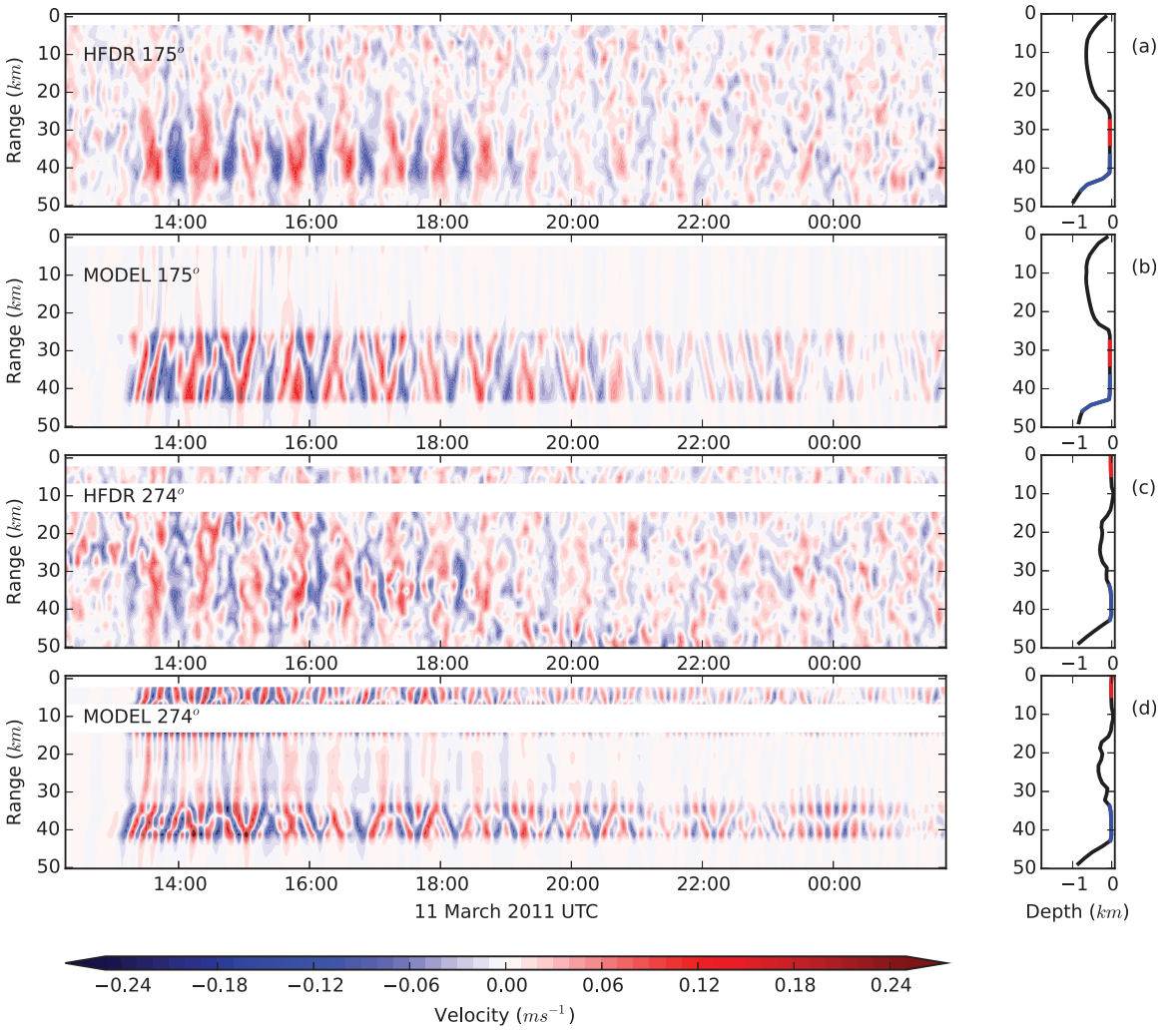

Figure 3. Filtered radial current velocity with distance from site as ordinate and time as abcissa: (a, b) for the 175° azimuth, which crosses Penguin Bank; (c, d) for the 274° azimuth, near the shore. The corresponding bathymetry is shown in the right. The boundary between the north and south Penguin Bank areas (red and blue in the bathymetry, respectively) is about 30 km from the HFDR. East nearshore and west nearshore are shown in red and blue in the bathymetry.

times the ocean Bragg wavelength, L (half the radio wavelength). As Δf is limited by the spectral resolution $1/T$ for record length T, the theoretical velocity resolution is L/T, or 0.07 m s^{-1} for this HFDR. Radial velocity v_b was actually computed as the weighted mean inferred directly from the backscatter spectra over an interval centered on the maximum amplitude of the Bragg scatter, $v_b = < vP(v) > / < P(v) >$. The velocity therefore appears as a continuous variable, having finer resolution than the theoretical resolution based on record length. The spatial range-resolution was 1.5 km and the beam width was 11°. KOK has 121 angular cells and 54 range cells, with 96% of the data available between 13:00 UTC on 11 March and 01:00 UTC on 12 March. Missing data points in space or time were interpolated. A low-pass Hamming finite impulse response (FIR) filter with a 3 dB cutoff at 8 min was applied forward and backward to all HFDR data to reduce noise, while a high-pass Hamming FIR filter with a 3 dB cutoff at 200 min was applied to remove the tides and other lower-frequency motions (e.g., near-inertial motions, Kelvin waves).

The Non-hydrostatic Evolution of Ocean Wave (NEOWAVE) model, developed by *Yamazaki et al.* [2009, 2011b], describes the Tohoku tsunami from its generation at the earthquake source to the coastlines of Hawaii. Because the model includes a nonhydrostatic pressure term and a shock-capturing scheme, it can model weakly dispersive waves and flow discontinuities associated with steep slopes, tsunami bores, and hydraulic jumps. The NEOWAVE model results have been validated at basin and coastal scales using DART buoys, tide gauges, bottom-mounted pressure sensors, and ADCPs [*Yamazaki et al.*, 2011a, 2012, 2013; *Cheung*

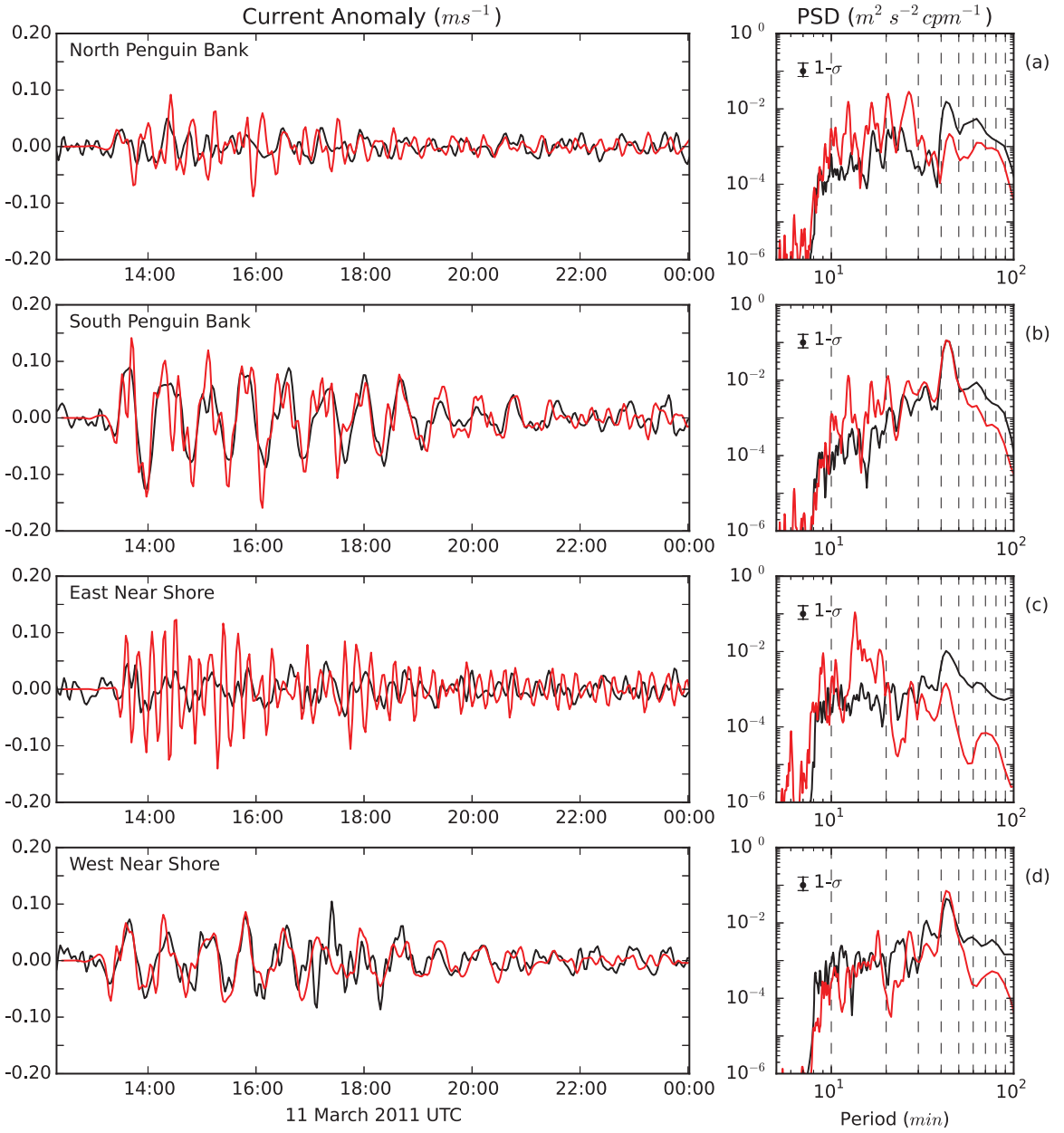

Figure 4. Radial velocity averaged along the 175° azimuth over the (a) north Penguin Bank and (b) south Penguin Bank areas, as well as along the 274° azimuth over the (c) east nearshore and the (d) west nearshore areas. The KOK HFDR is in black and NEOWAVE model data are in red. PSDs are shown to the right.

et al., 2013; *Bai et al.*, 2015]. Modeled, depth-integrated currents for the HFDR coverage areas were taken from *Cheung et al.* [2013]. The model's arrival time as measured by the initial peak was about 6 min early relative to the HFDR, possibly due to variations in water density and the elasticity of the Earth that are not taken into account [*Tsai et al.*, 2013; *Watada*, 2013]. The model data set was shifted 6 min to correct this difference. The model data at 1 min, 24 arcsec resolution was regridded to match the spatial and temporal sampling of the KOK HFDR, and the velocity vectors from the model were projected onto the radial directions of the HFDR. The same high-pass and low-pass FIR filters were applied to the model currents for consistence in the comparison.

Sea level sampled at 1 min from the Honolulu harbor tide gauge and from the DART buoy 51407, ~225 km southeast of Honolulu (Figure 1), were used to identify the tsunami's arrival time and benchmark the NEOWAVE results for comparison. Sea level data were subject to the same FIR filtering schemes.

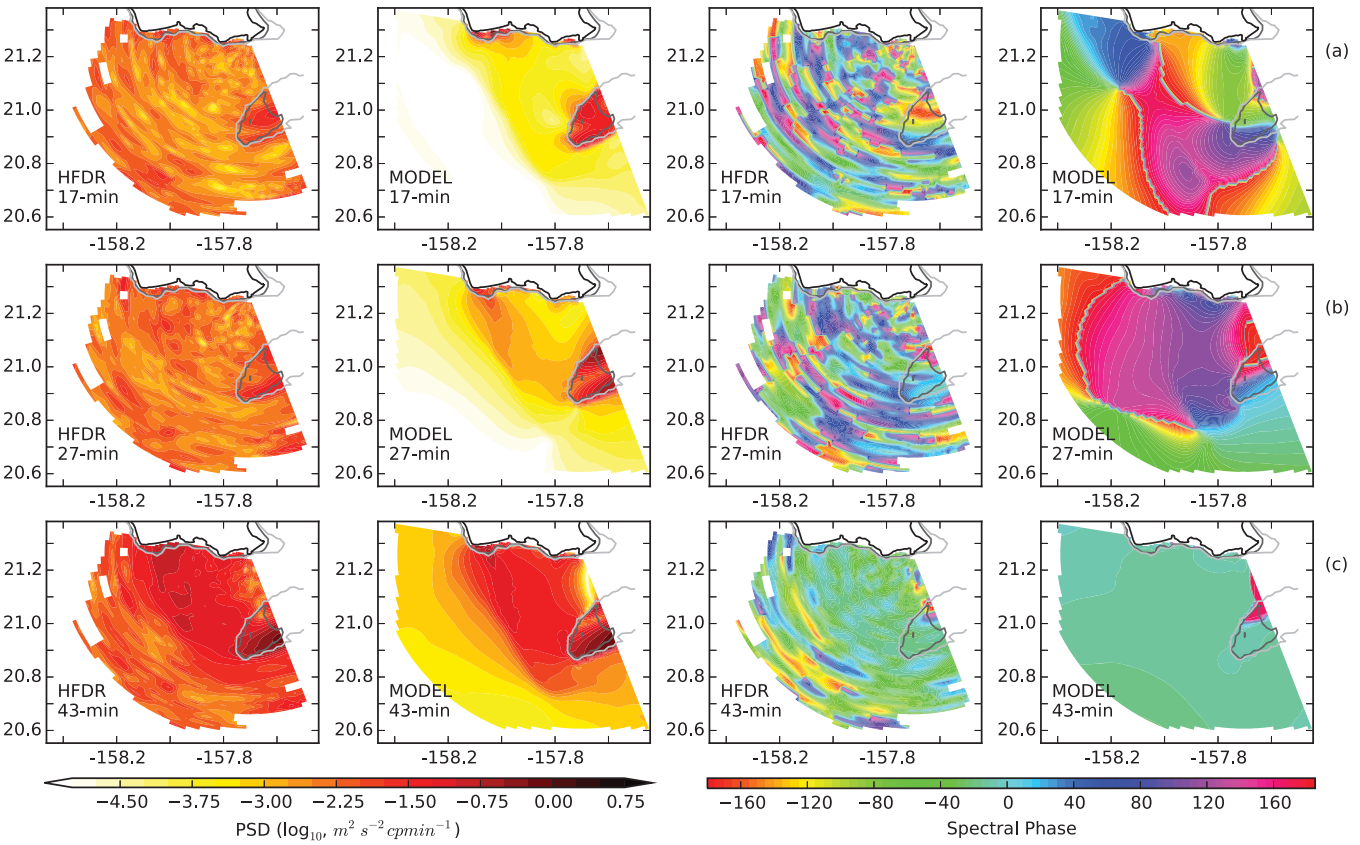

Figure 5. (first and second column) Power spectral density and (third and fourth column) phase for HFDR and model at (a) 17, (b) 27, and (c) 43 min periods. PSDs are scaled logarithmically and spectral phases are referenced to the first tsunami wave.

Fourier transforms were performed after windowing with a tapered cosine function and zero-padding the time series. Power spectral densities (PSDs) were computed as the energy per frequency band over the record time. The power spectral densities were smoothed by averaging adjacent bins, every other bin being independent. The spectral variances are χ^2-distributed with two degrees of freedom. Windowing and spectral smoothing alter the degrees of freedom to ∼12. The $1-\sigma$ error on the power spectra is found from the inverse χ^2 cumulative distribution. Spectral phases were determined by the argument of the original Fourier transform.

Empirical orthogonal function (EOF) analysis was performed over subset areas of the HFDR coverage during the first ∼12 h of the tsunami to find the dominant spatial modes and their temporal series over the entire domain; this procedure and the various motives are defined in the appendix. Correlations between the time series of EOF modes and raw data were examined for leakage between modes.

3. Results and Discussion

The peak of the initial tsunami wave reached south of Oahu at 13:17 UTC on 11 March, with near-simultaneous arrivals at the Honolulu tide gauge and the DART (Figure 2). Energetic oscillations are observed in both data sets, although the amplitude at Honolulu is nearly 3 times that of the DART. The observations and model match well in amplitude, phase, and periods of spectral peaks. The long-period oscillations at Honolulu continue with little damping until 18:00. The smaller, short-period oscillations dampen more quickly. There are few short-period oscillations present in DART data, and the long-period oscillations begin to attenuate around the same time as those at Honolulu. The peak period of the oscillations for both the DART and the tide gauge is 43 min. *Munger and Cheung* [2008] found a strong 43 min mode of oscillation covering the entire archipelago in the aftermath of the 2006 Kuril Islands tsunami. *Cheung et al.* [2013] numerically showed that the eigenmodes for Honolulu Harbor, a semienclosed harbor and the location of the Honolulu tide gauge, are 10.5 and 15 min, similar to the ∼10 and 16 min waves in the tide gauge data. The 27 min mode around

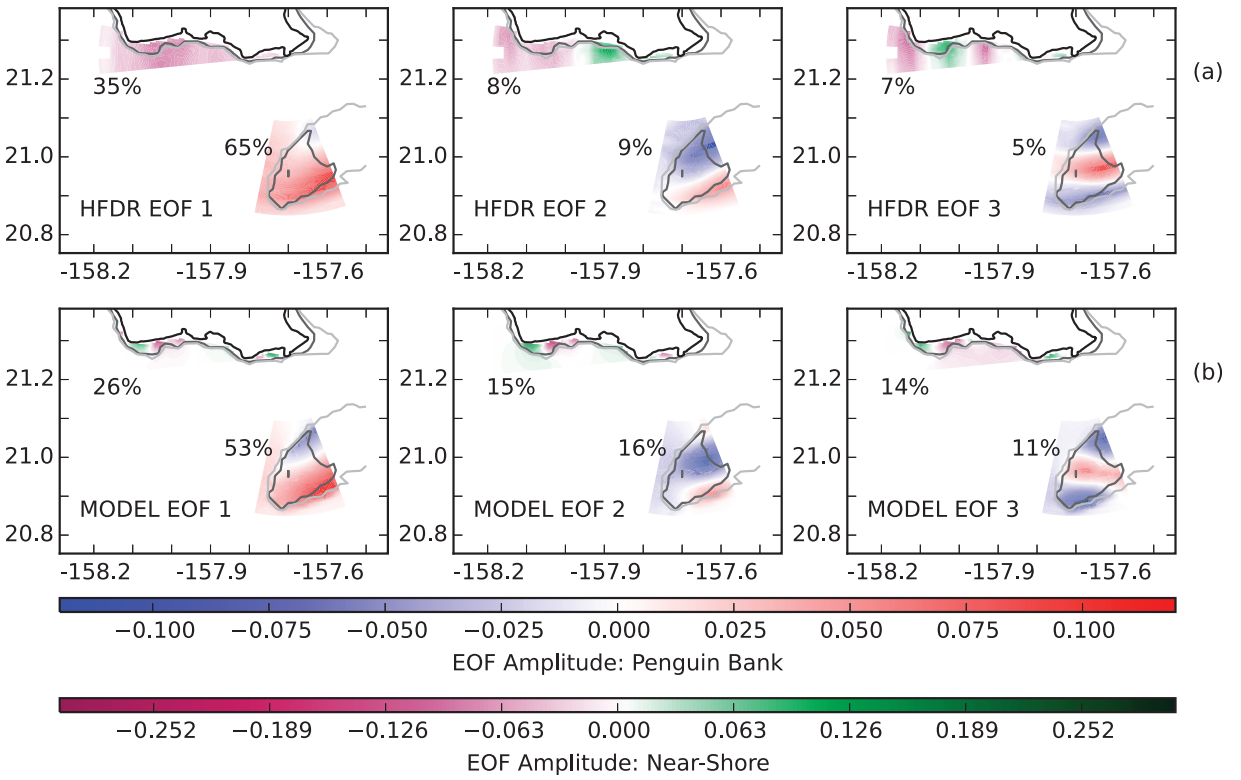

Figure 6. The first three EOF maps for (a) HFDR and (b) model data for the Penguin Bank area (608 grid points) and the nearshore area (595 grid points), with the percent variance for each mode. The EOFs are orthonormal and have not been scaled to reflect the number of grid points.

Molokai, Lanai, and Maui over their common shelves [*Cheung et al.*, 2013] may also have leaked into Honolulu Harbor, based on the spectral peak at 27 min in the tide gauge data.

The tsunami arrival is marked by energetic oscillations over Penguin Bank (Figures 3a and 3b), where particle velocities are amplified over shallow bathymetry. The HFDR data show north-south asymmetry of magnitude and duration of the oscillations over the bank: stronger and longer lasting south of the bank than north (−0.16 to 0.15 m s^{-1} for 6+h versus −0.08 to 0.09 m s^{-1} lasting ∼2 h). The regularity in the timing of the oscillations in the HFDR data on the southern part of the bank suggests standing waves. Typical filtered currents away from the bank are −0.02 to 0.02 m s^{-1}. In the model, the northern and southern flanks of the bank are not separated from one another, the asymmetry in strength being less prominent (−0.22 to 0.26 m s^{-1} south, −0.21 to 0.20 m s^{-1} north).

The arrival of the tsunami nearshore is marked in the HFDR data by a weak long-period current and in the model by stronger currents in two shallow regions: one near the HFDR site to the east, and one near the western point of the south shore (Figures 3c and 3d). These anomalous nearshore currents originate in the west and move eastward, with their direction reversing periodically, suggesting excitation of edge waves [*Bricker et al.*, 2007], that are not resolved by the HFDR. At ∼14:00, interference patterns emerge from the regular progression of edge waves, implying the presence of waves propagating in the opposite direction. The current strength drops ∼15:30 and vanishes ∼18:00 in the east, 21:00 in the west.

The radial currents spatially averaged in the north along the 175° HFDR azimuth do not display good agreement (Figure 4a). The modeled currents oscillate until ∼16:15 before decaying. The largest peak in the modeled currents is at 27 min. For the currents averaged in the south (Figure 4b), there is good agreement in period and amplitude for the entire interval shown. The peak at 43 min agrees well, but smaller peaks in the model spectrum at 13, 20, and 27 min are absent in the HFDR.

In the 274° nearshore direction, the currents averaged in the west (Figure 4d) show some agreement between HFDR observations and model results, but this is a spatial average over traveling features. In the east (Figure 4c), there are very different current patterns and no agreement. The spectra for the currents in the west agree only at the dominant 43 min period, while there is no agreement in the east.

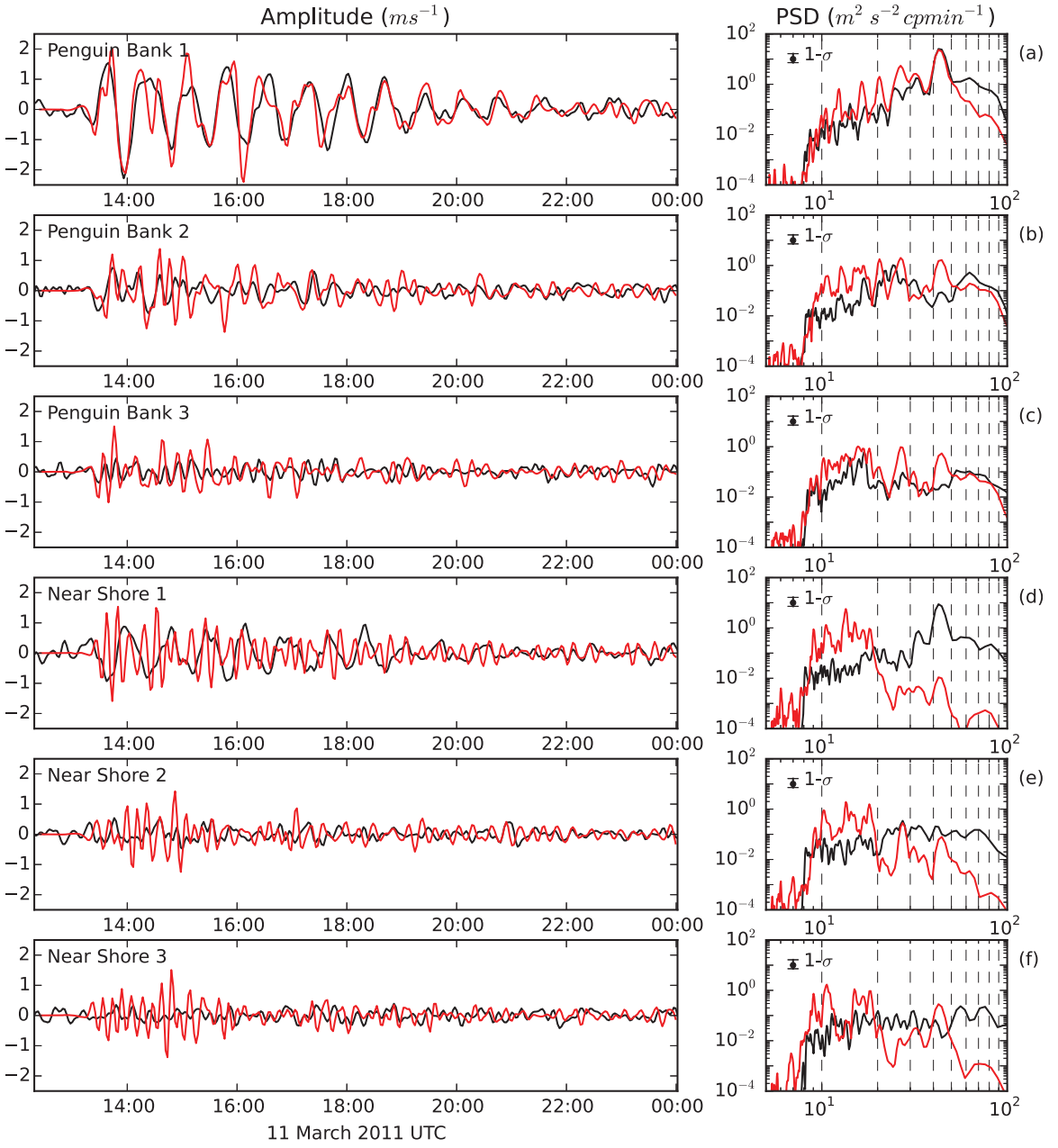

Figure 7. The time series (matrix $\mathbf{F}=\mathbf{V}^T\mathbf{D}$, see appendix) for the first three EOF modes for (a–c) Penguin Bank and (d–f) nearshore. HFDR is denoted in black and the model is in red. Spectra are at right.

Spectral amplitude maps show that Penguin Bank is a location of enhanced activity of periodic currents (Figure 5, columns 1, 2). HFDR spectral amplitudes in the north are weaker than in the south but in the model they have comparable strength. HFDR currents have a nodal line across the bank that is not as distinct as in the model.

The EOF maps over Penguin Bank for HFDR and model are similar (Figures 6a, 6b, and 7a–7c). The first modes contain 65% and 53% of the HFDR and model variance, respectively, and show opposing radial currents over Penguin Bank. Their time series show good phase and amplitude agreement, and the peaks at 43 min agree well. The second modes contain 9% and 16% of the HFDR and model variance, respectively, and, while also having opposing currents over the bank, the locations of the maxima are displaced relative to the first modes. The amplitudes and phases of the EOF time series do not agree, nor do the spectral peaks.

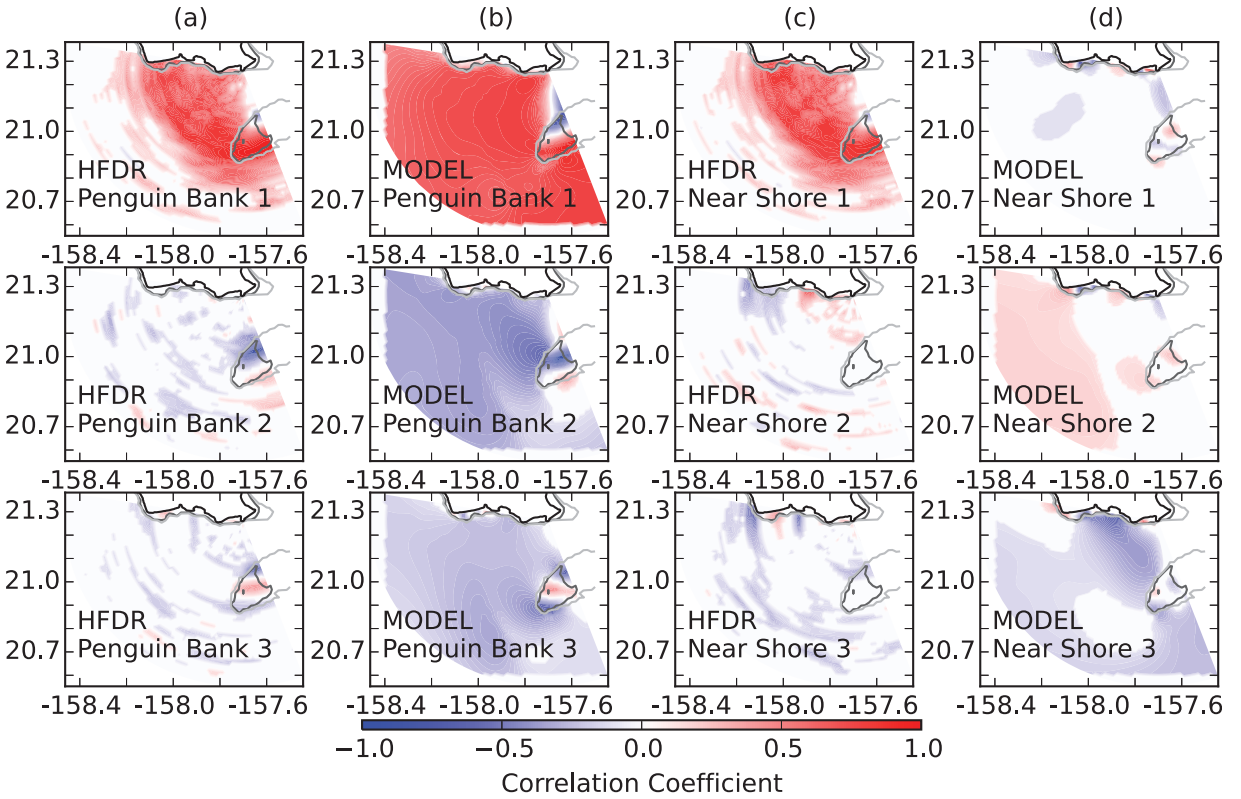

Figure 8. (a, b) Correlation between the time series of EOFs (matrix $\mathbf{F}=\mathbf{V}^T\mathbf{D}$, see appendix) computed over the Penguin Bank subset area and the data over the entire domain; (c, d) same, for EOFs computed over the nearshore subset area.

The third modes contain 5% and 11% of the HFDR and model variance, respectively, and have strong currents over north and south of the bank in the same direction, with a region of opposing current in between. The amplitudes and phases in the EOF time series do not match for this mode, nor do the periods of oscillation. The presence of two or more areas of opposing currents over Penguin Bank with distinct periods of oscillation suggests that these EOFs represent standing waves in surface elevation, with nodes and antinodes where the EOF maps are extreme and zero, respectively.

The model EOF maps near the shore have small features located along the coast, while the features in the HFDR are larger and extend farther (up to 10 km more) from the coast (Figures 6a and 6b). There are only weak similarities between HFDR and NEOWAVE modes 3. None of the EOF time series or their spectra shows any agreement between model and HFDR (Figures 7d–7f).

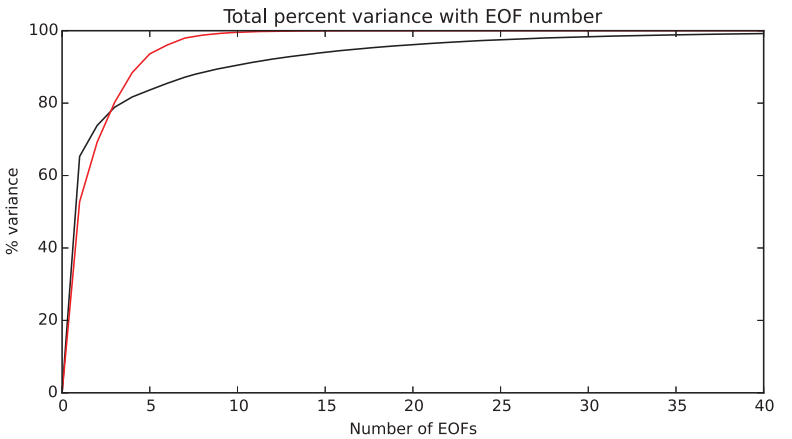

Figure 9. Total percent variance with number of EOFs. The model is denoted in red, and the HFDR is denoted in black.

Correlation coefficients between the HFDR EOF time series and HFDR observations (or model EOF time series and hindcast) show linkages between nearshore oscillations and Penguin Bank (Figure 8). The first HFDR modes both over Penguin Bank and in the nearshore (Figures 8a and 8c, top) are closely linked and expressed in deep waters, but the higher HFDR EOF modes are not. For the model, the Penguin Bank modes are strongly expressed over the entire coverage area, while the nearshore modes show weaker ties to Penguin Bank (Figures 8b and 8d). The high correlations for model modes over the whole domain that are not found in the HFDR modes are likely due to the absence of noise in the model. Instrument noise adds a component to the observations that is uncorrelated with the modes, while the absence of noise in the model allows the small oscillations in deep water to have a strong correlation with the EOF modes. The PSD (Figure 5) for deeper waters is 2 orders of magnitude smaller than that of Penguin Bank or nearshore due to weaker currents there, and the smoothness of the PSD and phase maps of the model relative to the HFDR highlight the absence of noise in the model. A plot of the cumulative percent variance explained versus the number of EOF modes included (Figure 9) shows that the initial three EOFs for both model and HFDR explain roughly 80% of the variance, but the model needs 10 modes to explain 99.5% of the variance while more than 40 are needed for the HFDR, possibly due to random measurement noise in the HFDR and the low resolution of the HFDR instrument.

Both Penguin Bank and the nearshore region are at the edges of the coverage area for the HFDR, where the azimuthal resolution is the worst. This degradation in resolution is visible in the HFDR nearshore EOF maps (Figure 6a), spectral amplitude maps (Figure 5, column 1), and regression coefficient maps (Figures 8a and 8c) as angular smearing of currents. The arcing of the maximum of spectral amplitude at 43 min over Penguin Bank toward the nearshore region may be enhanced by azimuthal sidelobe contamination or mapping of currents into an angle other than where they occur because of strong sidelobes.

4. Conclusions and Recommendations

The HFDR currents over Penguin Bank indicated that standing waves formed, including 43 min oscillations coincident with those in the nearshore HFDR data, the Honolulu tide gauge data, and DART 51407 data. The strongest component of currents in the HFDR and model matched well over Penguin Bank, and the major spectral and EOF modes showed good spatial agreement. Nearshore, a long-period, widespread oscillation was seen in both HFDR and model, but evidence for edge waves in the model was lacking in the HFDR. Disagreements between HFDR and the model primarily occurred where there was high spatial uncertainty due to either decreased angular resolution at high HFDR beam steering angles or azimuthal sidelobe contamination, or when the current magnitudes were too weak combined with the low resolution of the HFDR.

The EOF modal decomposition over Penguin Bank, which acts as a "probe" for resonance around the Hawaiian Islands, suggests a new method for now-casting the resonance amplitude of tsunamis. By projecting the high-passed real-time data from two or more HFDRs, preferably placed to minimize the dilution of precision over Penguin Bank (i.e., on the SE shore of Oahu and on the west shore of Molokai), into the predetermined EOF eigenvector base, a real-time index of tsunami current amplitude could be implemented. This index would not only yield a better monitoring of the risks of tsunami currents around the islands, but also allow the possible detection of resonance excited by processes other than earthquake waves, such as "meteo-tsunamis" excited by rapid meteorological phenomena [see *Lipa et al.*, 2013].

Appendix A: EOF Calculation and Scaling

EOF analysis rotates a set of time series in hyperspace such that the new EOF time series are uncorrelated. This is done by first finding an orthonormal basis that can describe the data in physical space the most efficiently (i.e., using the fewest vectors), and then transforming the data into the new basis to find the uncorrelated time series [*Lorenz*, 1956; *Richman*, 1986].

EOFs were computed over subset areas of interest, such as Penguin Bank or nearshore Oahu. The data are **D**, an $n \times t$ matrix with n as the number of grid positions and t as the number of time steps, and its covariance is **C**, an $n \times n$ matrix defined as

$$\mathbf{C}=\frac{1}{t-1}\mathbf{D}\mathbf{D}^T \tag{A1}$$

The factor of $\frac{1}{t-1}$ is required for an unbiased estimate of both variance and the covariance matrix.

Using the covariance method, the eigenvalue problem is posed as

$$\mathbf{C}\mathbf{V}=\mathbf{V}\Lambda \tag{A2}$$

in which Λ is the diagonal eigenvalue matrix and $\mathbf{V}$ is the $n \times n$ orthonormal eigenvector matrix, i.e., $\mathbf{V}^T\mathbf{V}=\mathbf{I}$. Rearranging (2) for just one $n\times1$ eigenvector E_i and one eigenvalue λ_i,

$$\mathbf{C}E_i=\lambda_i E_i \tag{A3}$$

$$(\mathbf{C}-\lambda_i\mathbf{I})E_i=\vec{0} \tag{A4}$$

The existence of a nontrivial solution to this problem requires that

$$det(\mathbf{C}-\lambda_i\mathbf{I})=0 \tag{A5}$$

After solving for the eigenvalues, the eigenvectors are found from (A4). Then, the $n \times t$ matrix $\mathbf{F}$ of the time series of the eigenvectors is

$$\mathbf{F}=\mathbf{V}^T\mathbf{D} \tag{A6}$$

The correlation matrix can then be rewritten as

$$\mathbf{C}=\frac{1}{t-1}\mathbf{D}\mathbf{D}^T=\frac{1}{t-1}\mathbf{V}\mathbf{F}\mathbf{F}^T\mathbf{V}^T \tag{A7}$$

Therefore,

$$\Lambda=\frac{1}{t-1}\mathbf{F}\mathbf{F}^T \tag{A8}$$

Unbiased variance eigenvalues contain the $\frac{1}{t-1}$ factor as well, consistent with (A2) and (A8). Eigenvalues and eigenvectors were computed using the singular value decomposition algorithm, or SVD.

The subset areas and times used to calculate the EOFs influence the resulting modes. Selecting the area over Penguin Bank, and the first 12 h of the tsunami, isolates this specific process. Increasing or decreasing the period over which the EOF is calculated reduces or increases the amount of variance in each mode, but their spatial structure does not significantly change.

Acknowledgments

The authors express their gratitude to Klaus-Werner Gurgel, whose 2011 paper provided the inspiration for the analysis presented, and who designed the algorithms used to extract the tsunami currents from the HFDR data. The authors would like to thank Matt Archer, Becky Baltes, Michael Brown, Jake Cass, Ken Constantine, Xavier Flores-Vidal, David Harris, Tyson Hilmer, Paul Lethaby, Philip Moravcik, Chris Ostrander, and Charina Repollo for assistance in the installation and maintenance of the Koko Head HFDR and Yefei Bai for assistance with the NEOWAVE model. The WERA HFDR, manufactured by Helzel Instruments, was loaned by Reginaldo Durazo of the Universidad Autónoma de Baja California. Funding for the installation and operation of the HFDR is provided by the Department of Homeland Security and the Pacific Islands Ocean Observing System (PacIOOS, http://pacioos.org), a component of NOAA's Integrated Ocean Observing System (IOOS) (award NA11NOS0120039). Contribution 9546 of the School of Ocean and Earth Science and Technology.

References

Allan, J. C., P. D. Komar, P. Ruggiero, and R. Witter (2012), The March 2011 Tohoku tsunami and its impacts along the U.S. West Coast, *J. Coastal Res.*, *28*(5), 1142–1153, doi:10.2112/JCOASTRES-D-11-00115.1.

Bai, Y., Y. Yamazaki, and K. F. Cheung (2015), Interconnection of multi-scale standing waves across the Pacific Basin from the 2011 Tohoku Tsunami, *Ocean Modell.*, *92*, 183–197, doi:10.1016/j.ocemod.2015.06.007.

Barrick, D. E. (1979), A coastal radar system for tsunami warning, *Remote Sens. Environ.*, *8*, 353–358.

Borrero, J. C., R. Bell, C. Csato, W. DeLange, D. Goring, S. D. Greer, V. Pickett, and W. Power (2013), Observations, effects, and real time assessment of the March 11, 2011 Tohoku-oki tsunami in New Zealand, *Pure Appl. Geophys.*, *170*, 1229–1248, doi:10.1007/s00024-012-0492-6.

Bricker, J. D., S. Munger, C. Pequignet, J. R. Wells, G. Pawlak, and K. F. Cheung (2007), ADCP observations of edge waves off Oahu in the wake of the November 2006 Kuril Islands tsunami, *Geophys. Res. Lett.*, *34*, L23617, doi:10.1029/2007GL032015.

Cheung, K. F., Y. Bai, and Y. Yamazaki (2013), Surges around the Hawaiian Islands from the 2011 Tohoku tsunami, *J. Geophys. Res. Oceans*, *118*, 5703–5719, doi:10.1002/jgrc.20413.

Dunbar, P., H. McCullough, G. Mungov, J. Varner, and K. Stroker (2011), 2011 Tohoku earthquake and tsunami data available from the National Oceanic and Atmospheric Administration/National Geophysical Data Center, *Geomatics Nat. Hazards Risk*, *2*(4), 305–323, doi:10.1080/19475705.632443.

Dzvonkovskaya, A., D. Figueroa, K.-W. Gurgel, H. Rohling, and T. Schlick (2011), HF radar WERA observation of a tsunami near Chile after the recent Great Earthquake in Japan, paper presented at International Radar Symposium IRS 2011, IEEE Aerospace and Electronic Systems Society, Leipzig, Germany.

Fiedler, J. W., M. A. McManus, M. S. Tomlinson, E. H. D. Carlo, G. R. Pawlak, G. F. Steward, O. D. Nigro, R. E. Timmerman, P. S. Drupp, and C. E. Ostrander (2014), Real-time observations of the February 2010 Chile and March 2011 Japan tsunamis recorded in Honolulu by the Pacific Islands Ocean Observing System, *Oceanography*, *27*(2), 186–200, doi:10.5670/oceanog.2014.36.

Grilli, S. T., S. Grosdidier, and C.-A. Guérin (2015), Modeling of tsunami detection by high frequency radar based on simulated tsunami case studies in the Mediterranean Sea, paper presented at ISOPE 2015 International Conference, ISOPE, Kona, Hawaii.

Gurgel, K.-W., H.-H. Essen, and S. P. Kingsley (1999a), High-frequency radars: Physical limitations and recent developments, *Coastal Eng.*, 37, 201–218.

Gurgel, K.-W., G. Antonischki, H.-H. Essen, and T. Schlick (1999b), Wellen radar (WERA): A new groundwave HF radar for ocean remote sensing, *Coastal Eng.*, *37*, 219–234.
Gurgel, K.-W., A. Dzvonkovskaya, T. Pohlmann, T. Schlick, and E. Gill (2011), Simulation and detection of tsunami signatures in ocean surface currents measured by HF radar, *Ocean Dyn.*, *61*, 1495–1507, doi:10.1007/s10236-011-0420-09.
Hinata, H., S. Fujii, K. Furukawa, T. Kataoka, M. Miyata, T. Kobayashi, M. Mizutani, T. Kokai, and N. Kanatsu (2011), Propagating tsunami wave and subsequent resonant response signals detected by HF radar in the Kii Channel, Japan, *Estuaries Coastal Shelf Sci.*, *95*, 268–273, doi:10.1016/j.ecss.2011.08.009.
Kaistrenko, V., N. Razjigaeva, A. Kharlamov, and A. Shishkin (2013), Manifestation of the 2011 Great Tohoku Tsunami on the coast of the Kuril Islands: A tsunami with ice, *Pure Appl. Geophys.*, *170*, 1103–1114, doi:10.1007/s00024-012-0546-9.
Lipa, B., D. Barrick, J. Bourg, and B. Nyden (2006), HF radar detection of tsunamis, *J. Oceanogr.*, *62*, 705–716.
Lipa, B., D. Barrick, S. Saitoh, Y. Ishikawa, T. Awaji, J. Largier, and N. Garfield (2011), Japan tsunami current flows observed by HF radars on two continents, *Remote Sens.*, *3*, 1663–1679, doi:10.3390/rs3081663.
Lipa, B., J. Isaacson, B. Nyden, and D. Barrick (2012), Tsunami arrival detection with high frequency radar, *Remote Sens.*, *4*, 1448–1461, doi:10.3390/rs4051448.
Lipa, B., H. Parikh, D. Barrick, H. Roarty, and S. Glenn (2013), High-frequency radar observations of the June 2013 US East Coast meteotsunami, *Nat. Hazards*, *74*(1), 109–122, doi:10.1007/s11069-013-0992-4.
Lorenz, E. N. (1956), Empirical orthogonal functions and statistical weather prediction, *Sci. Rep. 1*, Dep. of Meteorol., MIT, Vancouver, B. C., Canada.
Lynett, P., R. Weiss, W. Renteria, G. D. L. T. Morales, S. Son, M. E. M. Arcos, and B. T. MacInnes (2013), Coastal impacts of the March 11th Tohoku, Japan tsunami in the Galapagos Islands, *Pure Appl. Geophys.*, *170*, 1189–1206, doi:10.1007/s00024-012-0568-3.
Mimura, N., K. Yasuhara, S. Kawagoe, H. Yokoki, and S. Kazama (2011), Damage from the Great East Japan Earthquake and Tsunami—A quick report, *Mitigation Adaptation Strategies Global Change*, *16*, 803–818, doi:10.1007/s11027-011-9297-7.
Mori, N., T. Takahashi, T. Yasuda, and H. Yanagisawa (2011), Survey of the 2011 Tohoku earthquake tsunami inundation and run-up, *Geophys. Res. Lett.*, *38*, L00G14, doi:10.1029/2011GL049210.
Munger, S., and K. F. Cheung (2008), Resonance in Hawaii waters from the 2006 Kuril Islands Tsunami, *Geophys. Res. Lett.*, *35*, L07605, doi:10.1029/2007GL032843.
National Police Agency of Japan (2011), *Damage Situation and Police Countermeasures Associated With 2011 Tohoku District—Off Pacific Ocean Earthquake*, Emergency Disaster Countermeasures Headquarters, Tokyo, Japan. [Available at http://www.npa.go.jp/archive/keibi/biki/higaijokyo_e.pdf.]
Richman, M. B. (1986), Rotation of principal components, *J. Climatol.*, *6*, 293–335, doi:10.1002/joc.3370060305.
Roeber, V., Y. Yamazaki, and K. F. Cheung (2010), Resonance and impact of the 2009 Samoa tsunami around Tutuila, American Samoa, *Geophys. Res. Lett.*, *37*, L21604, doi:10.1029/2010GL044419.
Tsai, V. C., J.-P. Ampuero, H. Kanamori, and D. J. Stevenson (2013), Estimating the effect of Earth elasticity and variable water density on tsunami speeds, *Geophys. Res. Lett.*, *40*, 492–496, doi:10.1002/grl.50147.
Watada, S. (2013), Tsunami speed variations in density-stratified compressible global oceans, *Geophys. Res. Lett.*, *40*, 4001–4006, doi:10.1002/grl.50785.
Yamazaki, Y., and K. F. Cheung (2011), Shelf resonance and impact of near-field tsunami generated by the 2011 Chile earthquake, *Geophys. Res. Lett.*, *38*, L12605, doi:10.1029/2011GL047508.
Yamazaki, Y., Z. Kowalik, and K. F. Cheung (2009), Depth-integrated, non-hydrostatic model for wave breaking and run-up, *Int. J. Numer. Methods Fluids*, *61*(5), 473–497, doi:10.1002/fld.1952.
Yamazaki, Y., T. Lay, K. F. Cheung, Y. Hue, and H. Kanamori (2011a), Modeling near-field tsunami observations to improve finite-fault slip models for the 11 March 2011 Tohoku earthquake, *Geophys. Res. Lett.*, *38*, L00G15, doi:10.1029/2011GL049130.
Yamazaki, Y., K. F. Cheung, and Z. Kowalik (2011b), Depth-integrated, non-hydrostatic model with grid nesting for tsunami generation, propagation, and run-up, *Int. J. Numer. Methods Fluids*, *67*(12), 2081–2107, doi:10.1002/fld.2485.
Yamazaki, Y., K. F. Cheung, G. Pawlak, and T. Lay (2012), Surges along the Honolulu coast from the 2011 Tohoku tsunami, *Geophys. Res. Lett.*, *39*, L09604, doi:10.1029/2012GL051624.
Yamazaki, Y., K. F. Cheung, and T. Lay (2013), Modeling of the 2011 Tohoku near-field tsunami from finite-fault inversion of seismic waves, *Bull. Seismol. Soc. Am.*, *103*(2B), 1444–1455, doi:10.1785/0120120103.
Zhou, H., Y. Wei, L. Wright, and V. V. Titov (2014), Waves and currents in Hawaiian waters induced by the dispersive 2011 Tohoku tsunami, *Pure Appl. Geophys.*, *171*(12), 3365–3384, doi:10.1007/s00024-014-0781-3.